

A global study of Type B quasi-periodic oscillation in black hole X-ray binaries

H.Q. Gao^{1,2}, Liang Zhang³, Yupeng Chen¹, Zhen Zhang^{1,2}, Li Chen^{3*}, Shuang-Nan Zhang¹,
Shu Zhang¹, Xiang Ma¹, Zi-Jian Li^{1,2}, Qing-Cui Bu³, JinLu Qu^{1†}

¹Key Laboratory for Particle Astrophysics, Institute of High Energy Physics, CAS, 19B Yuquan Road, Beijing, 100049, P. R. China

²University of Chinese Academy of Sciences, 19A Yuquan Road, Beijing 100049, P.R. China

³Department of Astronomy, Beijing Normal University, Beijing 100875, P. R. China.

Accepted 2016 XX XX. Received 2016 XX XX

ABSTRACT

We performed a global study on the timing and spectral properties of type-B quasi-periodic oscillations (QPOs) in the outbursts of black hole X-ray binaries. The sample is built based on the observations of *Rossi X-ray Timing Explorer*, via searching in the literature in RXTE era for all the identified type-B QPOs. To enlarge the sample, we also investigated some type-B QPOs that are reported but not yet fully identified. Regarding to the time lag and hard/soft flux ratio, we found that the sources with type-B QPOs behave in two subgroups. In one subgroup, type-B QPO shows a hard time lag that firstly decreases and then reverse into a soft time lag along with softening of the energy spectrum. In the other subgroup, type-B QPOs distribute only in a small region with hard time lag and relatively soft hardness. These findings may be understood with a diversity of the homogeneity showing up for the hot inner flow of different sources. We confirm the universality of a positive relation between the type-B QPO frequency and the hard component luminosity in different sources. We explain the results by considering that the type-B QPO photons are produced in the inner accretion flow around the central black hole, under a local Eddington limit. Using this relationship, we derived an mass estimation of 9.3 – 27.1 M_⊙ for the black hole in H 1743-322.

Key words: accretion, accretion discs – black hole physics – X-rays: binaries – stars: black holes – stars: oscillations – colours, luminosities, masses, radii, temperatures

1 INTRODUCTION

A black hole X-ray binary (BHXB) is a gravitationally bound system consisting of a stellar mass black hole (BH) and a companion star. They are observed and characterized by their X-ray band, spectral and timing properties. Cygnus X-1, the first X-ray binary system (Webster & Murdin 1972) found for holding a BH, so far 24 sources have been clarified as BHXBs, and a similar number of sources were speculated as the possible BHXB candidates (see Zhang 2013; Remillard & McClintock 2006 for reviews). Most of BHXBs are transients, which usually stay in quiescence and show occasional outbursts in X-rays. An outburst usually shows evolution of different states defined with the peculiar spectral/timing properties, which are found to be well correlated

with the outflow features observed in forms of the jet and/or the disk wind. (see Fender & Belloni 2012 for review).

The systematic evolution of these states can be identified by their X-ray spectral and timing properties (see Zhang 2013; Remillard & McClintock 2006 for reviews). It had been known that the energy spectra of outbursting black holes often exhibit X-ray composite spectra consisting of two broadband X-ray components (Tanaka & Lewin 1995). A geometrically thin, optically thick accretion disk (Shakura & Sunyaev 1973) is thought to be the origin of the soft X-ray component and this thermal disk is thought to be the main structure in the high soft state (HSS). There is little doubt that the hard X-ray component is produced with the process of inverse Compton scattering, although the region for the Comptonising is still a matter of debate. It may be a covering layer above the disk (Haardt & Maraschi 1991; Haardt & Maraschi 1993), or some structures above the black hole as a wind or a jet base (Markoff, Nowak & Wilms 2005; Miller et al. 2006), or

* chenli@bnu.edu.cn (Li Chen)

† qujl@ihep.ac.cn (JinLu Qu)

outflows moving away from the disk (Beloborodov 1999; Malzac, Beloborodov & Poutanen 2001). In the truncated disk model (Esin, McClintock & Narayan 1997; Done et al. 2007) the thin disk truncates at some radius larger than the last stable orbit and is replaced by another kind of inner flow: a hot, optically thin accretion flow which acts as both the Comptonising region and the jet base.

In the transition between the low hard state (LHS) and the HSS, the hard component begins to be replaced by the soft component. Unlike the spectral properties that the hard state evolves continuously and smoothly to soft state in the hard intensity diagram (HID), abrupt changes within such an evolution are clearly observed and lead to a so-called isolate state, which can be distinguished to mark the separation of transition/intermediate state. So in the spectral hardness (the flux ratio between two different energy bands) root-mean-square(rms) diagram (HRD), a line-like single path consists of a low hard state, a Hard-Intermediate state (HIMS), a high soft state and an isolate island. In this spectral evolution, the soft-intermediate state (SIMS) occurs near the end of HIMS and stands for the beginning of the HSS (see Belloni 2010 for a review of this state classification). In the SIMS both the soft and hard components have high luminosity. The inner disk temperature is high and the hard component presents a steep energy spectrum. The accretion structure is very unclear in this state.

During the outburst, low-frequency quasi-periodic oscillations (QPOs; LFQPOs) with mHz to about 10 Hz are usually found. The *Rossi X-ray Timing Explorer* (RXTE) mission provided the large database of observations of the power density spectrum (PDS) containing LFQPO in many BHXBs and led to a significant progress in our knowledge on their timing properties. Now three main types of LFQPOs (type A, B and C) that were identified in XTE J1550-564 originally (see Wijnands et al. 1999; Homan et al. 2001; Remillard et al. 2002) widely present in other BHXBs (see van der Klis 2006; Belloni 2010 for reviews). The type C QPOs have a variable centroid frequency in the range of 0.1 - 15 Hz and a quality factor Q ($\nu/FWHM$) larger than 6. The PDS has a strong flat-top noise and the integrated fractional root-mean-squared (rms) amplitude is larger than 10%. Type-B QPOs have the frequency of about 1 - 8 Hz and Q larger than 6. The PDS shows a weak power-law noise and the integrated fractional rms amplitude is lower than 10%. Type A QPOs always follow type-B QPO in the HID and show PDS similar to type-B QPO but with broader QPO ($Q \leq 3$) and weaker amplitude (rms $\leq 5\%$). Since this classification of LFQPO solely considers their intrinsically differences in PDS (centroid frequency, quality factor, noise shape and variability level), it has the advantage of being phenomenological and model-independent and hence can be used in different BHXBs and even in Z sources of neutron star systems for probing their QPO analogy (Casella et al. 2005).

Most of the BHXB LFQPOs are found in the transition where the hard component steepens in energy spectrum and gradually give up the dominance along with the growing up of a more luminous thermal spectral component. In the HIMS, type C QPOs present. Their frequencies continue to increase, then change to type-B QPOs with a drop of the overall level of noise amplitude, when the source enters the SIMS (Belloni 2010; Motta et al. 2011). The appearance of

strong type-B QPOs is an indicator of the HIMS-SIMS transition (Belloni 2010) and a key entrance to the HSS for an entire ‘q’ track outburst (Zhou et al. 2013). It is also observed with the ‘jet line’ and may be associated with the ‘moment of jet launch’ (Soleri et al. 2008; Fender et al. 2009; Miller-Jones et al. 2012). The type-B QPOs occur just at the moment of the transition of X-ray energy spectral states, behaving in phenomenon of a sharp change of timing properties and radio jet events, which is usually believed to associate with the evolution of the accretion flow and the launching of outflow.

In GX 339-4, Motta et al. (2011) reported type-B QPOs observed following a different pattern in the QPO frequency versus hard flux compared with type C and type A QPOs. Gao et al. (2014) studied the type-B QPOs of GX 339-4 sample and suggested that they may result from the blob related ejection event that have indeed intrinsically different properties from the type C QPOs. In GRO J1655-40, Motta et al. (2012) reported a type-B QPO and a type C QPO observed simultaneously in a very luminous state, suggesting they have intrinsically different properties. In the truncated disk scenario (Done et al. 2007), type C QPO is thought to be produced from the Lense-Thirring precession (Stella & Vietri 1998) of the misaligned inner hot flow and the band-limit noise component comes from propagation of magnetorotational instability of the same inner hot flow. The frequency of QPO mainly relays on the truncation radius (Ingram et al. 2009, Ingram & Done 2010 and Ingram & Done 2011). The peculiar properties of type-B QPOs suggest their different origins with respect to type C QPO (Motta et al. 2011, Motta et al. 2012). Rapid transitions among type-B to type-A QPOs are observed in GX 339-4 (Motta et al. 2011), XTE 1817-330 (Sriram et al. 2012) and XTE J1859+226 (Sriram et al. 2013), showing with evolution of the disk parameters derived from energy spectral fittings (Sriram et al. 2013). These results suggest that type-B and A QPOs may originally share more similarity than type-B and C QPOs. In GX 339-4, the type-B QPO appearance in the SIMS is always accomplished with a peak in count rate (Motta et al. 2011) and a flare in hard component flux, indicating the source spectral state returning from HSS to SIMS. This result may suggest that there is a sudden input of seed photons for up-compton scattering in the hot flow (Gao et al. 2014). These abrupt seed photons may reform a small isotropic and spherical sharp inner hot flow structure, after the previous inner hot flow consumption in the LHS to HSS transition. However, the underline physics corresponding to the appearance of SIMS and the accompanied type-B QPO is not yet quite clear and is speculated to tightly relate to the formation mechanism of type-B QPO.

In this paper, based on the richness of the literature and the large database of RXTE, we will try to build a sample of type-B QPOs from all the BHTs to study the type-B QPOs with a view of global phenomena among different BHXB systems, which have different BH masses, distances and inclinations. In Section 2, we show the sample selection and outline the data analysis procession. The results are given in Section 3, and the discussions are in Section 4.

2 DATA SAMPLE AND ANALYSIS

We examined all the RXTE archival observations of all the black hole X-ray transients. For each observation, we obtained the good time interval (GTI) using the criteria of elevation angle ($ELV \geq 10^\circ$), offset $\leq 0.02^\circ$, and the South Atlantic Anomaly (SAA) passage time (also see Gao et al. (2014)). The observations with $GTI \geq 100$ s were selected as our observation sample.

2.1 The sample

In order to get a global type-B QPO, the power density spectrum was produced for each observational sample and the type-B QPOs were chosen following the definition of Casella et al. (2005). The results are then compared with the literatures (which are listed in the Tab. 1) that reported type-B QPOs. However, Motta et al. (2015) provided a complete LFQPO sample derived from RXTE observations that contain 135 type-B QPOs. We use it to check our type-B QPOs sample. Finally, in our sample, the total number of type-B QPOs is 99. The exclusions and some notes are given in what follows.

1, The source GRS 1915+105 is excluded for its unusual outburst evolution behavior and complex light-curve (Belloni et al. 2000).

2, We focus on the type-B QPOs in the rising phase of outbursts. The lower frequency type-B QPO in the decay phase is excluded, which ends up with 8 for GX 339-4 and 4 for H 1743-322.

3, GRO J1655-40 was reported with type-B QPO together with a type C QPO in its PDS (Motta et al. 2012). There are also some other sources holding this similar phenomenon at the peak luminosity (Li, Z. B. et al. 2014). Although they share some similar properties of type B QPO PDS, their energy spectra and states are significantly different from SIMS type-B QPOs; we also do not take these ones into our sample for uniformity. We also exclude those similar observations in 4U 1630-47.

4, Some of type-B QPO in Motta et al. (2015) are inconclusive for us which makes it hard to put them into standard type-B QPO class. Although they are surly not type C or type A QPO, by comparing to other normal type-B QPOs, they are remarkably distinguished by their band-limit noise shapes.

Finally, there are eight unusual type-B QPOs in the HSS of XTE J1817-330 during its 2006 outburst. In our sample, they are classified into type-B QPOs because of their weak powerlaw red noise and sharp QPO quality factor. We treat them as unusual type-B QPOs because they also show the similarity with type A QPO in that the rms has lower values. The HSS of this outburst is also unusual. It was reported with a higher inner disk temperature (0.8-0.9 keV) and a harder spectral component (Γ 2.1-2.3) than other usual HSS of BHXBs (Roy et al. 2011; Sriram et al. 2012).

2.2 Data analysis

For our timing analysis, we used Event, Binned, Single-Bit and Good Xenon data modes. The PDS was produced for each observation using POWSPEC version 1.0 task of the XRONOS package in the channel band 0-35. We divided the data into 64 s segments with 8 ms time resolution. The PDS

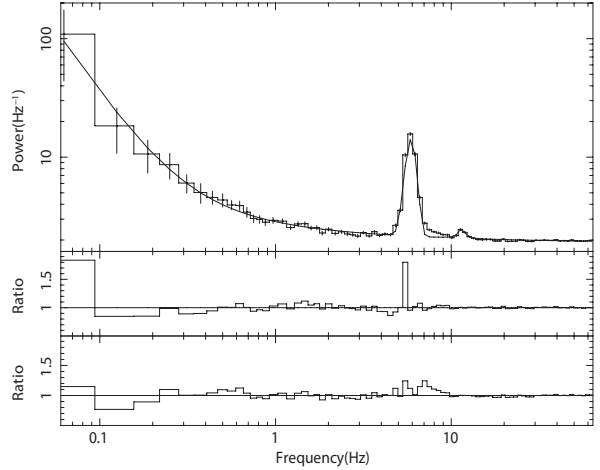


Figure 1. Typical type-B QPO power density spectrum from GX 339-4. The two lower panels show the ratio residuals of models using a Lorentzian and a Gaussian to fit the QPO component, respectively.

was computed for each segment and averaged with the logarithmic rebin in frequency. The PDS was normalized using Miyamoto method (Miyamoto et al. 1991) and the Poisson noise was subtracted. For all the type-B QPO profile in PDS, we found that Gaussian can provide a better fitting (see Fig. 1). This is also confirmed by Motta et al. (2011). So we used a power-law component for red noise and a Gaussian component for the type QPO to get QPO frequency, FWHM and QPO normalization in PDS from the best fit. We calculated time/phase lags by means of the cross-power spectrum (CPS) analysis following Qu et al. (2010), Cui et al. (1997) and Nowak (1994). The cross-power spectrum (CPS) is $C(j) = X_1^*(j)X_2(j)$, where $X_i(j)$ is the complex Fourier coefficient for energy band i at a given frequency f_j . The position angle of the cross vector C in the complex plane (the Fourier phase $\phi(j) = \arg[C(j)]$) are the phase lags between the two energy bands. The time lags are $\phi(j)$ divided by $2\pi f_j$. The time/phase lags of type-B QPO component were calculated by averaging the cross vector $C(j)$ at the QPO centroid frequency over the frequency range of the QPO FWHM. The errors were estimated through the standard deviation of the real and imaginary parts of the CPSs (Cui et al. 1997). We chose two broad channel bands of 0-13 (2-5.7 keV) and 14-35 (5.7-14.8 keV) to estimate the time/phase lags between low and high energy photons of the type-B QPO sample.

The energy spectra were extracted and fitted from background and dead-time-corrected PCA (Jahoda et al. 1996) and HEXTE (Rothschild et al. 1998) data observation using FTOOLS v6.12 and XSPEC v12.7 (Arnaud 1996). PCA spectra were extracted only from Standard 2 mode data born out of PCA/PCU2 and the HEXTE spectra from HEXTE/Cluster B. Considering the HEXTE/Cluster B encountered technical problems at the end of 2009, for type-B QPO observations in 2010 outburst of GX 339-4, HEXTE data were produced following Motta et al. (2011). For the type-B QPO observations in 2010 and 2011 outburst of H 1743-322, the HEXTE data were not used because of the large incorrect estimation in the background transformation from Cluster B to A. A Gaussian Fe-K emission line with

Table 1. List of black hole transients with type-B QPOs

System	Outbursts	BH Mass (M_{\odot})	Inclination (deg)	Distance (kpc)	N_{H} ($\times 10^{22} \text{ cm}^{-2}$)	Number of type-B QPO Obs.
4U 1543–47	2002	9.4 ± 2.0 (1)	20.7 ± 1.5 (2)	7.5 ± 0.5 (3)	0.43 (3)	3 (4)
GX 339–4	2002, 2004, 2007, 2010	5.8 ± 0.5 (5)	≥ 40 (6)	8.0 ± 4.0 (7)	0.5 (7)	26 (8)
XTE J1752–223	2009	9.6 ± 0.9 (9)	≤ 49 (10)	3.5 ± 0.4 (9)	0.46 (11)	1 (9)
XTE J1817–330	2006	4.0 ± 2.0 (12)		5 ± 4 (12)	0.15 (12)	8
XTE J1859+226	1999	10.0 ± 5.0 (13)	≥ 60 (14)	6.2 ± 1.8 (15)	0.34 (15)	14 (4,16)
XTE J1550–564	1998	10.6 ± 1.0 (2)	74.7 ± 3.8 (17)	$4.38^{+0.58}_{-0.41}$ (17)	0.65 (18)	11 (4,19)
H 1743–322	2003, 2009, 2010, 2011	unknown	75 ± 3 (20)	8.5 ± 0.8 (20)	2.4 (21)	32 (4,22,23,24)
MAXI J1659–152	2010	$3.6 - 8.0$ (25)		$5.3 - 8.6$ (25)	0.17 (25)	4 (4)

(1) Ritter & Kolb (2003), (2) Orosz et al. (2002), (3) Jonker & Nelemans (2004), (4) Motta et al. (2015), (5) ?, (6) Muñoz-Darias et al. (2008), (7) Zdziarski et al. (2004), (8) Motta et al. (2011), (9) Shaposhnikov et al. (2010), (10) Miller-Jones et al. (2011), (11) Markwardt et al. (2009), (12) Sala et al. (2007), (13) Hynes et al. (2002), (14) Casella et al. (2011), (15) Hynes et al. (2003), (16) Casella et al. (2004), (17) Orosz et al. (2011), (18) Gierliński & Done (2003), (19) Remillard et al. (2002), (20) Steiner et al. (2012), (21) Capitanio et al. (2005), (22) Li, Z. B. et al. (2013), (23) Motta et al. (2010), (24) Zhou et al. (2013), (25) Yamaoka et al. (2012).

centroid energies allowed vary between 6.4 and 6.7 keV was needed to obtain the best fits. The line width is constrained to a range of 0.1 – 1.0 keV to prevent artificial broadening due to the response of XTE/PCA at 6.4 keV (Motta et al. 2011). In addition, an iron edge component was added when its inclusion improve the fits significantly. The value of the hydrogen column density ($wabs$) for different sources was fixed (the value and the reference in Tab. 1 N_{H} column). We took the model of *diskbb+powerlaw* to fit the combined PCA/HEXTE spectra in the energy ranges 3 - 40 keV and 20 - 200 keV, respectively and using the model of *cflux* to estimate the flux of each component in the energy ranges 2-30 keV. A systematic error of 0.6 percent was added to account for residual uncertainties of the instrument calibration (Motta et al. 2011). The best-fitting results have a reduced χ^2 between 0.85 and 1.7 in general and the error bars are of 2.7σ confidence level. The power-law index is in the range between 2.13 and 2.69 with an average value of 2.47 ± 0.04 , which is consistent with the value in the SIMS. As an example, we show the changes of the reduced χ^2 without/with Fe line and absorption edge in Fig. 2. And we report in Tab. 3 the frequency of the QPO, the inner disk temperature and power-law index of spectral fit for each observation.

3 RESULT

In Fig. 3, we plot the frequency of the type-B QPOs vs. the time lag. The energy band of PCA/RXTE used in time lag analysis is about 2-5.7 keV and 5.7-14.8 keV. A hard lag means that the hard photons lag the soft ones, while a soft lag means that the soft photons lag the hard ones. As shown in this figure, the time lag of the type-B QPOs distributes from ~ 10 ms hard lag to ~ 15 ms soft lag. Fig. 4 exhibits the relation of time lag and the ‘hardness ratio’ ($power - lawflux/diskflux$) of the type-B QPO. Two source subgroups can be distinguished from those data distribution. All the type-B QPOs of GX 339–4, 4U 1543–47 and XTE J1752–223 concentrate in the regions with a hard time lag of about 5-10 ms and a relatively small hardness ratio of about 0.4-0.7. We therefore define these sources as

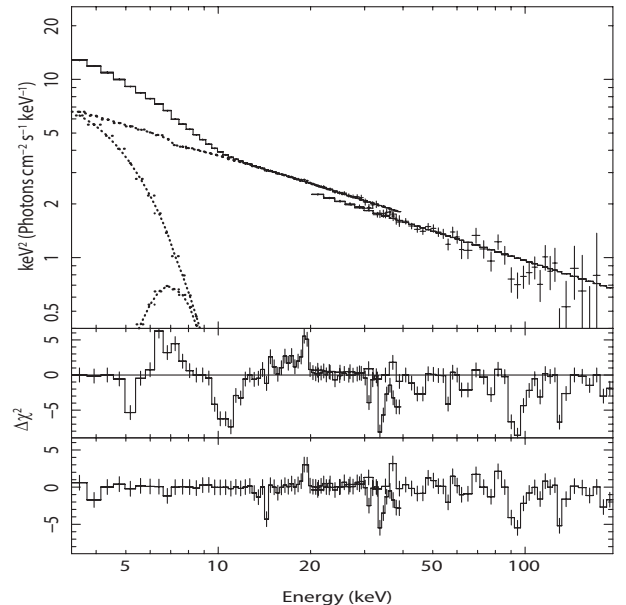


Figure 2. Typical PCA and HEXTE spectra of XTE J1859+226, fitted by a model with an absorbed disk blackbody and a power-law component. The two lower panels show the reduced- χ^2 without/with iron line and absorption edge respectively.

subgroup 1 sources. Most of type-B QPOs in this region are from the single source GX 339–4, scattering into four different outbursts. The rest of type-B QPOs are from the other sources which have a very large range evolution in the time lag from hard time lag to soft time lag and a large hardness ratio change. These sources enclose H 1743–322, XTE J1859+226, XTE J1550–564, XTE J1817–330, MAXI J1659–152 and constitute subgroup 2. A clear relation established for subgroup 2 is that, along with decreasing in flux hardness ratio, the hard time lag decreases and then changes to 15 ms soft lag finally.

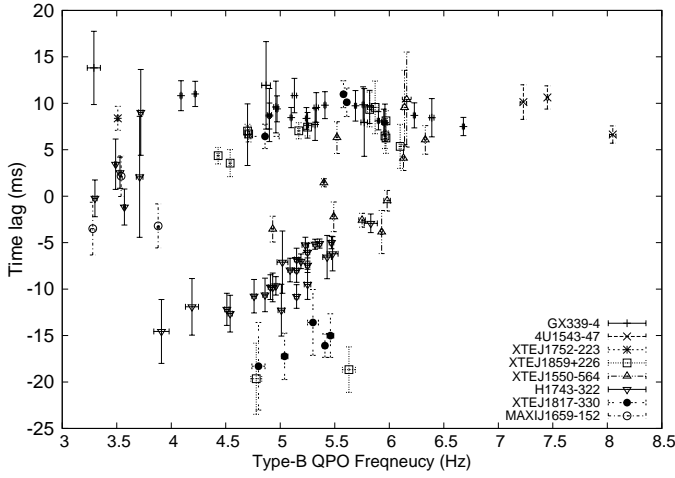


Figure 3. Type-B QPO frequency versus time lag.

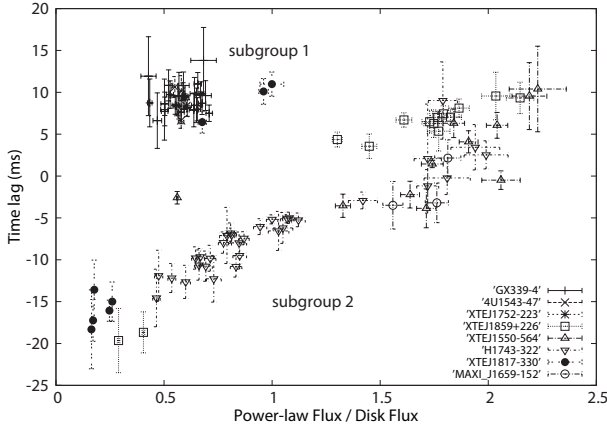


Figure 4. Type-B QPO hard time lag versus the ratio of power-law flux and disk flux.

Table 2. Time lag spectra for six observations with type-B QPO show in Fig. 5

obID	source	QPO frequency	time lag
95409-01-18-05	GX 339-4	4.92 ± 0.02	8.89 ± 2.56
92082-01-02-03	XTE J1817-330	4.89 ± 0.01	6.35 ± 1.15
40124-01-36-00	XTE J1859+226	4.70 ± 0.02	7.14 ± 0.61
30191-01-34-01	XTE J1550-564	4.92 ± 0.01	-3.93 ± 1.31
80146-01-56-00	H 1743-322	4.85 ± 0.02	-10.05 ± 1.58
91110-02-18-00	XTE J1817-330	5.02 ± 0.03	-15.06 ± 2.09

The type-B QPO observations show diverse shapes of time lag spectra. Fig. 5 shows the time lag spectra of six typical type-B QPO observations. We mark them with number 1 to 6 and list the further information in Tab. 2. We chose these type-B QPOs with the similar frequency in a narrow range of 4.7 to 5.0 Hz to minimize the influence of frequency difference. Fig. 5 shows that the time lag spectrum changes from number 1 to 6 following a trend of having firstly an increasing hard time lag and then evolving toward a decreasing soft time lag. Type-B QPO observations of number 2 and 6 are both from XTEJ1817-330. The result shows that they are intrinsically different in time lag spectrum shape.

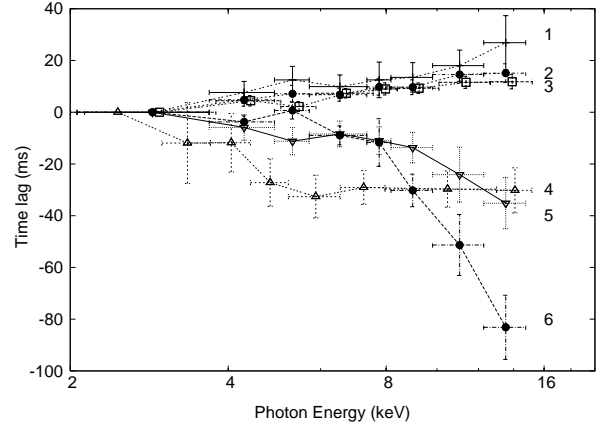


Figure 5. The time lag spectra of six typical type-B QPO observations. Points symbols are the same with other figures for different sources.

Type-B QPO observation number 3 is from XTEJ1859+226. Although in Fig. 4 it belongs to the subgroup 2, its time lag spectra show no significant difference with respect to the shape that characterizes the subgroup 1 (Number 1 of GX 339-4).

Fig. 6 shows the relations between the time lag and inner disk temperature of type-B QPOs observations. The type-B QPOs of subgroup 1 locate at the left top corner in the figure with a large hard time lag and a low inner disk temperature. One type-B QPO (Number 2) of XTE J1817-330 also locates in the dense region of subgroup 1. The subgroup 2 points occupy the rest area with a larger dispersion, especially considering five other type-B QPOs of XTE J1817-330. The type-B QPOs from H 1743-322 2003 outbursts concentrate densely at the right bottom. In the middle, there exist a few type-B QPOs from XTE J1859+226, XTE J1550-564 and six type-B QPOs born out of outbursts of H 1743-322 during 2009-2011. There is a negative trend between the inner disk temperature and time lag, i.e., a hotter inner disk corresponds to a softer time lag of type-B QPOs, if we exclude the type-B QPOs of XTE J1817-330. The source XTE J1817-330 seems to behave in a different way in Fig. 6. Their time lags share two subgroups in the Fig. 4. The transition between hard and soft time lags suggests that there may exist a rapid change of the hot accretion flow in a timescale of several days. But We need to verify this via further observations in future.

Fig. 7 is the relation between the inner disk temperature and the frequency of type-B QPOs. Different symbols stand for the observations from different sources. The inner disk temperature shows a tendency of increase with the frequency of type B QPO. This relation can be found in GX339-4, XTE J1859+226, XTEJ1550-564 and XTEJ1817-330. The highest inner disk temperature of type-B QPO observations comes from H1743-322 (the hollow inverted triangle points around 1.2 keV). They distribute in a relatively crowded region and show no clear relation between inner disk temperature and the type-B QPO frequency. But by combining the additional six type-B QPO observations at about 0.95 keV, this relation still holds in H1743-322. Focusing on four sources with the largest number of SIMS type-B QPOs and the finest ABC confirmation, the energy ranges of inner disk

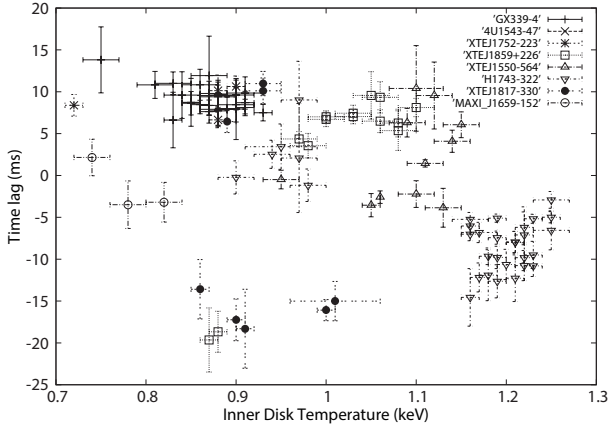


Figure 6. Type-B QPO hard time lag versus inner disk temperature.

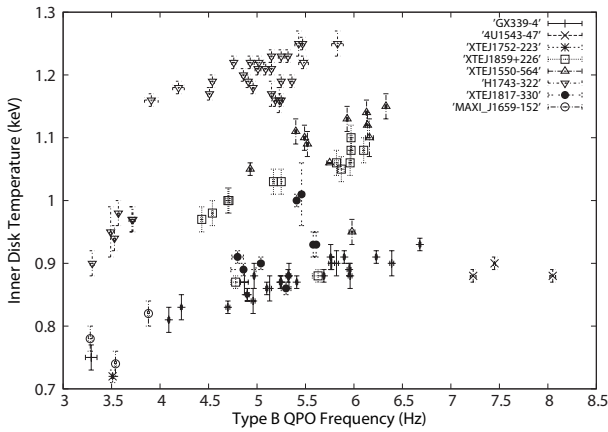


Figure 7. Type-B QPO frequency versus inner disk temperature.

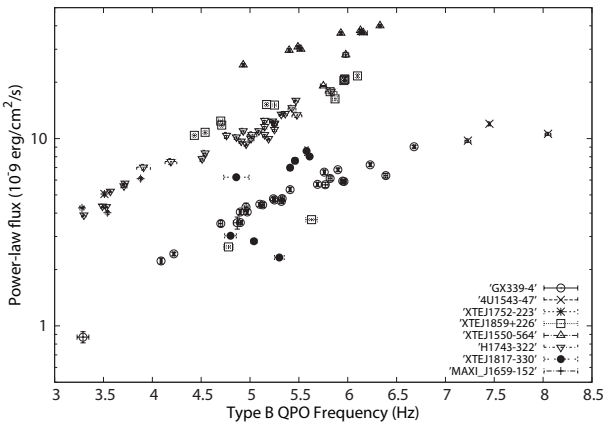


Figure 8. Type-B QPO frequency versus hard component flux.

temperature of type-B QPO observations are 0.99–1.24 keV (H1743-322), 0.91–1.10 keV (XTEJ1550-564), 0.84–1.01 keV (XTE J1859+226), 0.78–0.91 keV (GX 339-4), respectively. Within these four sources, the type-B QPOs of GX 339-4 have the lowest inner disk temperature in general.

Fig. 8 shows evolution of the type-B QPO frequency as a function of the hard component (power-law) flux. Whichever subgroup the source belongs to, the common positive rela-

tion between the type B QPOs frequency and the hard component flux stand out clearly (Fig. 8) in GX 339-4, XTE J1550-564, XTE J1859+226 and H 1743-322.

Fig. 9 shows evolution of the type-B QPO frequency as a function of the power-law luminosity (in units of Eddington luminosity). Here, the Eddington luminosity is $L_E = 1.3 \times 10^{38} (M/M_\odot) \text{ erg s}^{-1}$. The errors of the hard component Eddington luminosity mainly come from the uncertainty of the distance and black hole mass (We only show the typical error-bars caused by distance uncertainty of the source H 1743-322 and GX 339-4 for clarity). The positive relation of the hard component flux and frequency of type-B QPO points from three sources (GX339-4, XTE J1859+226 and XTE J1550-564) turns out to be in rather linear shape (solid square points in Fig. 9).

We should note that in Fig. 9 (left), we assumed a typical black hole mass of $10 M_\odot$ for H 1743-322 due to its mass is poorly known. The data points of H 1743-322 are located above and in parallel with the main relationship formed by other sources. We then adjusted the black hole mass of H 1743-322 to make its frequency-power-law Eddington luminosity relationship consistent with the main relationship. A black hole mass of 9.3-27.1 M_\odot was obtained in the 95% confidence level.

4 DISCUSSION

We discuss our results in the framework of truncated disk geometry (Done et al. 2007): the standard disk is truncated at a radius larger than the last stable orbit and replaced by a hot inner accretion flow. As the accretion rate increases, the inward movement of the truncation radius of disk corresponds to the gradual dominance of thermal disk. It leads to the cooling, consumption and even final collapse of the hot inner flow correlated with hard to soft state transition. The SIMS is a very narrow period of an outburst that is noticeable in the HID. During the transition of the LHS to HSS, the hard component steepens and begins to drop while the soft component becomes dominate. In the SIMS both of them are quite bright together with the appearance of type-B QPOs (Belloni 2010). They have been found in many different sources which have different mass, distance and inclination.

4.1 Time lag results

In the simple Comptonization process, the millisecond hard time lag comes from the delay in collisions of seed soft photons with the high energy electrons in the corona. The hard photons lag behind the soft photons because the hard photons undergo more scatters to gain energy (Nowak et al. 1999). It is consistent with the hard time lag of subgroup 1 sources' type-B QPOs in Fig. 4. However if the Comptonization region is homogenous and has a uniform temperature, no soft time lag can be produced. Nobili et al. (2000) propose a nonhomogeneous Compton cloud model to explain hard/soft time lag and the evolution between them with the decrease of hardness ratio observed in state C of GRS 1919+105. The seed photons are upscattered in the inner part region of the corona that has higher temperature and large scattering depths than the outer part of corona. The

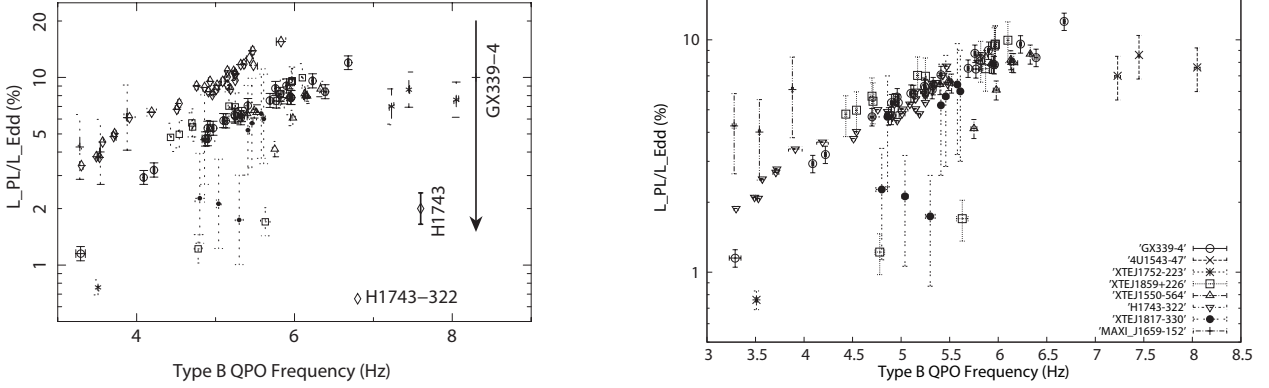


Figure 9. Hard component (Power-law) Eddington fraction versus type-B QPO frequency. The left panel is assuming 10 solar masses for H 1743–322. The typical distant error of GX 339–4 and H 1743–322 are shown. Points symbols are the same with right panel. The right panel is 18 solar masses for H 1743–322.

observed spectrum and soft lag are the effect that the photons are downscattered in the cooler and outer part of the corona. The relative change of disk-corona geometry and the hotter inner part and cooler outer part of corona itself leads to the soften of time lag and the decrease of hardness ratio. Three points cause the observed correlation: a nonhomogeneous corona, a truncated disk, and a source of more energetic primary photons from a smaller inner disk radius. It is consistent with the model proposed by [Nobili et al. \(2000\)](#).

Compared with the relation of time lag and hardness ratio of state C QPO in [Nobili et al. \(2000\)](#), the similar phenomena have been observed for subgroup 2 sources (H 1743–322, XTE J1550–564, XTE J1859+226 and XTE J1817–330 in Fig. 4) type-B QPOs in a larger range as a whole: the time lag changes from hard to soft together with the decrease of hardness. It suggests that they share the similar transfer time lag progress in a similar evolution of accretion flow circumstance: when the inner disk edge moves inward to the BH, the optical depth of the outer part of the non-homogeneous corona increases with the sharper gradient of temperature; downscattering process becomes more important with respect to upscattering in the corona. With the softening of the spectrum, the hard time lag decreases and even inverses to soft. Although the scenario of [Nobili et al. \(2000\)](#) was proposed for a single source, all the type-B QPOs are in the SIMS, which is a very narrow state in the HID and each source in subgroup 2 shows this evolution in a small range. The results combining different sources show some kind of large ‘evolution’ because of the intrinsic diversity of their accretion flow properties. The type-B QPOs of subgroup 1 sources do not show such time lag evolution; the hard/soft flux ratio varies slightly. It suggests that they have a more homogenous Comptonization region and the upscattering process dominates. In Fig. 5, all these six type-B QPO observations have the similar QPO frequency (see Tab. 2). The significant difference in the shape of time lag spectra of them suggest they have little relation with the QPO frequency producing mechanism. The oscillation photons undergo different scattering process after the type-B

QPO is produced at a certain frequency. The overall distribution of temperature from subgroup 1 is in the left top region in Fig. 6, which shows a lower inner disk temperature. It suggests that the subgroup 1 sources have weaker ability to provide enough energetic primary photons than subgroup 2. Considering that the sources of subgroup 2 are high inclination systems than subgroup 1 ([Muñoz-Darias et al. 2013](#); [Motta et al. 2015](#)), it may lead to a larger optical depth of the outer part of the nonhomogeneous corona in the line of sight and more temperature gradient, if the corona has a disk-like geometry. Perhaps the inclination effect is the reason to make corona homogeneous or not from the line of sight.

The propagating fluctuations model suggests that mass accretion rate fluctuations are generated over a wide range of radii corresponding to a wide range of time-scales. The fluctuations introduced at large radii are then propagate towards the black hole producing the observed variations in the X-ray flux ([Lyubarskii 1997](#)). Since the inner regions have a harder spectrum than the outer regions, the inward propagation of fluctuations naturally give rise to hard X-ray time lags ([Misra 2000](#); [Kotov et al. 2001](#)). Using this model, [Arévalo & Uttley \(2006\)](#) reproduced the expected $\sim 1/f$ frequency-dependence of time lags of Cyg X–1. However, [Uttley et al. \(2011\)](#) found that this model can explain the 2–3 vs. 0.5–0.9 keV hard lags of ~ 0.1 s or longer, but it fails to explain the short lags (several ms) observed in our results.

Type-B QPO frequencies clearly correlate with the power-law component flux, suggesting that this type QPO are more likely to be related to the presence of a jet ([Motta et al. 2011](#)). A jet model which describes that Compton upscattering of low-energy photons in the jet can produce the hard lags ([Reig et al. 2003](#); [Giannios et al. 2004](#); [Kylafis et al. 2008](#)). In this model, seed photons from the accretion disk are fed into the base of the jet not into a corona, and anisotropy of the scattering process along the jet can traverse large distances in the jet, to produce large lags of longer than 0.1 s ([Uttley et al. 2011](#)). We also should

note that both propagating fluctuations model and jet model are difficult to produce the soft lags observed in the type-B QPOs.

4.2 Spectra-timing correlation results

Among the type-B QPOs within each source, the inner disk temperature increases with the type-B QPO frequency (Fig. 7). The correlation of type-B QPOs frequencies with the power-law flux has been observed in GX 339–4 (Motta et al. 2011). In our result, this phenomenon has been observed in a more global sample including GX 339–4 and both subgroup 1 and 2 sources with the same frequency-hard component flux correlation (Fig. 8). This common tendency in different sources suggests that the mechanism of type-B QPO produced in the accretion flow share a common physical process. After normalization to Eddington luminosity, a tight linear relation among the type-B QPOs sample of GX 339–4, XTE J1859+226, XTE J1550–564 can be found together with H 1743–322; a higher frequency corresponds to a higher hard luminosity. It is a global and intrinsic property of type-B QPO that may come from its special accretion physics, which makes type-B QPO different from other type of QPOs.

In an local Eddington-limited thin disk, the disk is in the critical accretion state within a critical radius r_{cr} , and the maximum accretion rate in the inner disk region is much less than the classical Eddington value. The fractional critical accretion luminosity of disk corresponds to inner disk radius: $L/L_E \propto \ln \frac{r_{cr}}{r_t}$ (Fukue 2004; Heinzeller & Duschl 2007; Neilsen et al. 2011). L_E is the classical Eddington luminosity. Under the assumption that type-B QPOs are excited in the critical Eddington accretion related process, in the Lense-Thirring QPO interpretation, an approximate relation of the frequency and the truncation radius is $f \propto r_t^{-3}$ (Stella & Vietri 1998, van der Klis 2006 and Ingram et al. 2009). Combining them, the luminosity of the inner disk region and the type-B QPO frequency $L/L_E \propto \ln(f \times r_{cr})$. These inner disk photons are Comptonization upscattered in the hot inner flow. The positive relation of hard component Eddington luminosity and the type-B QPO frequency can be explained.

Under the assumption that the type-B QPO is produced by Lense-Thirring mechanism in the condition of local Eddington-limited, the intrinsic relation of type-B QPOs frequency and hard component Eddington fractional luminosity may provide us a new way to estimate the unknown mass of a black hole as a standard candle. The black hole mass of H 1743–322 is poorly known. Using the correlation between spectra index and QPO frequency, Shaposhnikov & Titarchuk (2009) obtained a mass value of 13.3 ± 3.2 . We estimate the mass of H 1743–322 and the most consistent result between 9.3 and 27.1 M_\odot . However, we should note that he derived mass of H1743–322 is both flux and frequency limited and may vary for a broad range of flux and frequency. And there are some disperse points in the Fig. 9. Our fitted results show the slopes of the linear function are consistent in the 95% confidence level when the disperse points included or excluded. The extension of type-B QPO sample and the development of the parameters measurement of known masses black holes will improve this method.

5 SUMMARY AND CONCLUSION

Within the RXTE data, we selected and studied 99 type-B QPOs from black hole X-ray binaries. We performed the timing and spectral properties study of them and discussed the results in the framework of truncated disk geometry.

(1) The time lag results show two subgroup behaviors. In subgroup 1, type-B QPOs distribute only in a small region with hard time lag and relatively soft hardness value. In subgroup 2, type-B QPOs show the hard time lag that decreases with soften of energy spectra and finally inverting to soft lag. The subgroup 2 sources correspond to a nonhomogeneous corona, which is different from subgroup 1 sources.

(2) In the spectrum-timing correlation results, we confirm the universality of the positive relation between the type-B QPOs frequency and the hard component luminosity in different sources. These results can be explained by that the type-B QPO photons are produced in the condition of local Eddington critical accretion of inner disk region. In case of having the Lense-Thirring QPO model at work, the type-B QPO frequency and luminosity would evolve jointly with the truncated disk radius, in a form of a positive relationship.

(3) Using the relation of hard component Eddington luminosity and the type-B QPOs frequency, we estimate the unknown mass of H 1743–322 and obtain a value between 9.3 and 27.1 M_\odot .

ACKNOWLEDGMENTS

The authors thank the RXTE team for making these data publicly available. The authors thank anonymous referee for some helpful suggestions and comments. This work is supported in part by the National Natural Science Foundation of China (11173024, 11133002, 11073021, 11473027, 11103020), XTP project XDA04060604, the Strategic Priority Research Program "The Emergence of Cosmological Structures" of the Chinese Academy of Sciences, Grant No. XDB09000000 and the Natural Science Foundation of China for Young Scientists (Grant No. 11203064). The National Basic Research Program (973 Program) of China (Grant No. 2014CB845800).

REFERENCES

- Arévalo P., Uttley P., 2006, MNRAS, 367, 801
- Arnaud K. A., 1996, ASPC, 101, 17
- Belloni T., Klein-Wolt M., Méndez M., van der Klis M., van Paradijs J., 2000, A&A, 355, 271
- Belloni T. M., 2010, Lecture Notes in Physics, Springer-Verlag Berlin Heidelberg, Volume 794, p. 53. ISBN 978-3-540-76936-1., 794, 53
- Beloborodov A. M., 1999, ApJ, 510, L123
- Capitanio F., Ubertini P., Bazzano A., et al., 2005, ApJ, 622, 503
- Casella P., Belloni T., Homan J., Stella L., 2004, A&A, 426, 587
- Casella P., Belloni T., Stella L., 2005, ApJ, 629, 403
- Corral-Santana J. M., Casares J., Shahbaz T., 2011, MNRAS, 413, L15
- Done C., Gierliński M., Kubota A., 2007, A&AR, 15, 1
- Esin A. A., McClintock J. E., Narayan R., 1997, ApJ, 489, 865
- Fender R. P., Homan J., Belloni T. M., 2009, MNRAS, 396, 1370
- Fender R., Belloni T., 2012, Sci, 337, 540

- Fukue J., 2004, PASJ, 56, 569
- Gao, H. Q., Qu, J. L., Zhang, Z., et al., 2014, MNRAS, 438, 341
- Giannios D., Kylafis N. D., Psaltis D., et al., 2004, A&A, 425, 163–171
- Gierliński M., Done C., 2003, MNRAS, 342, 1083
- Haardt F., Maraschi L., 1991, ApJ, 380, L51
- Haardt F., Maraschi L., 1993, ApJ, 413, 507
- Heinzeller, D., & Duschl, W. J., 2007, MNRAS, 374, 1146
- Homan J., Wijnands R., van der Klis M., Belloni T., van Paradijs J., Klein-Wolt M., Fender R., Méndez M., 2001, ApJS, 132, 377
- Hynes R. I., Haswell C. A., Shrader C. R., et al., 1998, MNRAS, 300, 64
- Hynes R. I., Haswell C. A., Chaty S., Shrader C. R., Cui W., 2002, MNRAS, 331, 169
- Hynes R. I., Steeghs D., Casares J., Charles P. A., O’Brien K., 2003, ApJ, 583, L95
- Ingram A., Done C., Fragile P. C., 2009, MNRAS, 397, L101
- Ingram A., Done C., 2010, MNRAS, 405, 2447
- Ingram A., Done C., 2011, MNRAS, 415, 2323
- Johoda K., Swank J. H., Giles A. B., et al., 1996, SPIE, 2808, 59
- Jonker P. G., Nelemans G., 2004, MNRAS, 354, 355
- Kotani T., Kawai N., Nagase F., et al., 2000, ApJ, 543, L133
- Kotov O., Churazov E., Gilfanov M., 2001, MNRAS, 327, 799
- Kylafis N. D., Papadakis I. E., Reig P., et al., 2008, A&A, 489, 481
- Li, Z. B., Zhang, S., Qu, J. L., Gao, H. Q., Zhao, H. H., Huang, C. P., Song, L. M., 2013, MNRAS, 433, 412
- Li, Z. B., Gao, H. Q., Zhang, Z., Zhang, S., Qu, J. L., Zhang, C. M., Song, L. M., 2014, MNRAS, 440, 143
- Lyubarskii Y. E., 1997, MNRAS, 292, 679
- Malzac J., Beloborodov A. M., Poutanen J., 2001, MNRAS, 326, 417
- Markoff S., Nowak M. A., Wilms J., 2005, ApJ, 635, 1203
- Markwardt C., Barthelmy S., Evans P., Swank J., 2009, ATel, 2261, 1
- McClintock J. E., Remillard R. A., 2006, in Lewin W. H. G., van der Klis M., eds, Compact Stellar X-Ray Sources. Cambridge Univ. Press, Cambridge, p. 157
- Miller J. M., Homan J., Steeghs D., Rupen M., Hunstead R. W., Wijnands R., Charles P. A., Fabian A. C., 2006, ApJ, 653, 525
- Miller-Jones J., Jonker P. G., Ratti E. M., et al., 2011, MNRAS, 415, 306
- Miller-Jones J., Sivakoff G. R., Altamirano D., et al., 2012, MNRAS, 421, 468
- Misra R., 2000, ApJ, 529, L95
- Miyamoto S., Kimura K., Kitamoto S., Dotani T., Ebisawa K., 1991, ApJ, 383, 784
- Motta S., Muñoz-Darias T., Belloni T., 2010, MNRAS, 408, 1796
- Motta S., Muñoz-Darias T., Casella P., Belloni T., Homan J., 2011, MNRAS, 418, 2292
- Motta S., Homan J., Muñoz-Darias T., Casella P., Belloni T., Hiemstra B., Méndez M., 2012, MNRAS, 427, 595
- Motta S., Casella P., Henze M., Muñoz-Darias T., Sanna A., Fender R., Belloni T., 2015, MNRAS, 447, 2059
- Muñoz-Darias T., Casares J., Martínez-Pais I. G., 2008, MNRAS, 385, 2205
- Muñoz-Darias T., Coriat M., Plant D. S., Ponti G., Fender R. P., Dunn R. J. H., 2013, MNRAS, 432, 1330
- Neilsen J., Remillard R. A., Lee J. C., 2011, ApJ, 737, 69
- Nobili L., Turolla R., Zampieri L., Belloni T., 2000, ApJ, 538L, 137N
- Nowak M. A., Vaughan B. A., Wilms J., Dove J. B., Begelman M. C., 1999, ApJ, 510, 874
- Orosz J. A., Polisenky E. J., Bailyn C. D., Tourtellotte S. W., McClintock J. E., Remillard R. A., 2002, in Bulletin of the American Astronomical Society, Vol. 34, 1124
- Orosz J. A., Steiner J. F., McClintock J. E., Torres M. A. P., Remillard R. A., Bailyn C. D., Miller J. M., 2011, ApJ, 730, 75
- Reig P., Kylafis N. D., Giannios D., 2003, A&A, 403, L15
- Remillard R. A., Sobczak G. J., Muno M. P., McClintock J. E., 2002, ApJ, 564, 962
- Remillard R. A., McClintock J. E., 2006, ARA&A, 44, 49
- Ritter H., Kolb U., 2003, A&A, 404, 301
- Rothschild R. E., Blanco P. R., Gruber D. E., et al., 1998, ApJ, 496, 538
- Roy J., Agrawal P. C., Paul B., Duorah K., 2011, MNRAS, 412, 1011
- Sala G., Greiner J., Ajello M., Bottacini E., Haberl F., 2007, A&A, 473, 561
- Shakura, N. I., & Sunyaev, R. A., 1973, A&A, 24, 337
- Shaposhnikov N., Markwardt C., Swank J., Krimm H., 2010, ApJ, 723, 1817
- Shaposhnikov N., Titarchuk L., 2009, ApJ, 699, 453
- Soleri P., Belloni T., Casella P., 2008, MNRAS, 383, 1089
- Sriram K., Rao A. R., Choi C. S., 2012, A&A, 541, A6
- Sriram K., Rao A. R., Choi C. S., 2013, ApJ, 775, 28
- Steiner J. F., McClintock J. E., Reid M. J., 2012, ApJ, 745, L7
- Stella L., Vietri M., 1998, ApJ, 492, 59
- Remillard R. A., McClintock J. E., 2006, ARA&A, 44, 49
- Tanaka Y., and Lewin W. H. G., "Black-hole Binaries", in X-ray Binaries, edited by W. H. G. Lewin, J. van Paradijs, and E. P. J. van den Heuvel, Cambridge U. Press, Cambridge, 1995, pp. 126-174.
- Uttley P., Wilkinson T., Cassatella P., et al., 2011, MNRAS, 414, L60
- Webster L., Murdin P., 1972, Nat, 235, 37
- Wijnands R., Homan J., van der Klis M., 1999, ApJ, 526, L33
- van der Klis M., 2006, Advances in Space Research, 38, 2675
- Yamaoka, K., Allured, R., Kaaret, P., et al., 2012, PASJ, 64, 32
- Zdziarski A. A., Gierliński M., Mikołajewska J., Wardziński G., Smith D. M., Harmon B. A., Kitamoto S., 2004, MNRAS, 351, 791
- Zhang S. N., 2013, FrPhy, 8, 630
- Zhou, J. N., Liu, Q. Z., Chen, Y. P., et al., 2013, MNRAS, 431, 2285

Table 3: QPO and best-fit spectral parameters from all the observations on the sources of our sample.

#	ID	Exposure (s)	Frequency (Hz)	kT_{in} (keV)	Γ	χ^2/ν
GX 339-4						
1	60705-01-84-02	1680	4.97 ± 0.01	0.84 ± 0.02	2.38 ± 0.04	1.10/74
2	70108-03-02-00	9888	5.32 ± 0.02	0.83 ± 0.01	2.53 ± 0.03	0.92/74
3	70109-01-07-00	5120	5.90 ± 0.01	0.88 ± 0.02	2.58 ± 0.05	0.77/74
4	70110-01-14-00	880	6.39 ± 0.02	0.87 ± 0.02	2.43 ± 0.04	0.98/74
5	70110-01-15-00	880	5.82 ± 0.02	0.87 ± 0.02	2.51 ± 0.05	1.21/74
6	70110-01-47-00	1200	5.77 ± 0.03	0.86 ± 0.02	2.57 ± 0.05	0.93/74
7	90110-02-01-03	1056	4.09 ± 0.01	0.78 ± 0.02	2.33 ± 0.07	0.82/74
8	90704-01-02-00	3104	4.22 ± 0.01	0.78 ± 0.02	2.31 ± 0.04	0.94/74
9	91105-04-10-00	704	3.29 ± 0.06	0.68 ± 0.04	2.22 ± 0.14	1.07/74
10	92035-01-04-00	3232	6.68 ± 0.01	0.91 ± 0.02	2.53 ± 0.03	0.44/47
11	92085-01-03-01	2304	6.23 ± 0.01	0.87 ± 0.02	2.51 ± 0.03	0.74/74
12	95335-01-01-00	3408	5.25 ± 0.01	0.83 ± 0.02	2.52 ± 0.03	0.71/74
13	95335-01-01-01	2976	5.10 ± 0.01	0.83 ± 0.02	2.53 ± 0.04	0.62/47
14	95335-01-01-05	1520	4.90 ± 0.01	0.82 ± 0.02	2.55 ± 0.05	0.87/47
15	95335-01-01-06	3440	4.90 ± 0.02	0.81 ± 0.01	2.50 ± 0.04	1.20/47
16	95335-01-01-07	1056	5.33 ± 0.02	0.85 ± 0.03	2.46 ± 0.06	0.58/47
17	95409-01-15-02	1344	5.76 ± 0.01	0.89 ± 0.02	2.52 ± 0.04	0.55/47
18	95409-01-15-06	1424	5.69 ± 0.01	0.85 ± 0.02	2.55 ± 0.04	0.68/47
19	95409-01-16-05	2880	5.95 ± 0.02	0.86 ± 0.02	2.46 ± 0.03	1.18/47
20	95409-01-17-00	960	5.96 ± 0.02	0.85 ± 0.02	2.45 ± 0.05	0.81/47
21	95409-01-17-05	2464	5.24 ± 0.01	0.84 ± 0.02	2.50 ± 0.04	0.81/47
22	95409-01-17-06	1216	5.13 ± 0.02	0.83 ± 0.02	2.51 ± 0.05	0.91/47
23	95409-01-18-00	1152	5.41 ± 0.01	0.83 ± 0.02	2.54 ± 0.05	0.61/47
24	95409-01-18-04	144	4.87 ± 0.04	0.85 ± 0.02	2.33 ± 0.14	0.57/47
25	95409-01-18-05	528	4.96 ± 0.02	0.82 ± 0.02	2.60 ± 0.08	0.66/47
26	95409-01-19-00	896	4.70 ± 0.02	0.80 ± 0.02	2.53 ± 0.07	1.04/47
4U 1543-47						
27	70133-01-11-00	1056	7.45 ± 0.01	0.86 ± 0.02	2.67 ± 0.03	0.88/74
28	70133-01-15-00	1184	8.05 ± 0.03	0.83 ± 0.02	2.50 ± 0.03	1.05/74
29	70133-01-16-00	864	7.23 ± 0.03	0.83 ± 0.02	2.57 ± 0.04	0.96/74
H 1743-322						
30	80135-02-02-00	5760	5.47 ± 0.02	1.24 ± 0.01	2.63 ± 0.03	0.68/74
31	80135-02-02-000	15776	5.32 ± 0.02	1.23 ± 0.01	2.68 ± 0.01	1.21/74
32	80135-02-02-01	1424	4.76 ± 0.02	1.20 ± 0.01	2.64 ± 0.07	0.95/74
33	80144-01-01-01	1376	5.43 ± 0.04	1.24 ± 0.01	2.65 ± 0.06	1.05/74
34	80144-01-01-02	1584	5.83 ± 0.06	1.23 ± 0.01	2.69 ± 0.03	0.89/74
35	80144-01-02-00	1952	5.25 ± 0.03	1.21 ± 0.02	2.61 ± 0.06	1.01/74
36	80144-01-02-01	1408	5.48 ± 0.05	1.18 ± 0.02	2.69 ± 0.04	0.68/74
37	80144-01-03-01	1488	5.01 ± 0.03	1.18 ± 0.02	2.67 ± 0.04	1.00/74
38	80146-01-51-00	3328	4.54 ± 0.02	1.16 ± 0.02	2.63 ± 0.03	0.76/74
39	80146-01-51-01	3328	4.19 ± 0.06	1.15 ± 0.02	2.58 ± 0.03	0.82/74
40	80146-01-52-00	3344	5.15 ± 0.02	1.22 ± 0.02	2.63 ± 0.05	0.88/74
41	80146-01-52-01	3424	5.09 ± 0.02	1.19 ± 0.01	2.55 ± 0.05	0.89/74
42	80146-01-53-00	2464	4.93 ± 0.02	1.19 ± 0.02	2.65 ± 0.06	1.10/74
43	80146-01-53-01	1296	5.02 ± 0.05	1.18 ± 0.03	2.67 ± 0.05	0.75/74
44	80146-01-54-00	5440	4.91 ± 0.02	1.17 ± 0.02	2.53 ± 0.05	1.13/74
45	80146-01-55-00	3220	5.15 ± 0.02	1.18 ± 0.02	2.66 ± 0.03	0.97/74
46	80146-01-56-00	2912	4.86 ± 0.02	1.17 ± 0.02	2.63 ± 0.04	0.83/74
47	80146-01-58-00	3392	3.91 ± 0.07	1.13 ± 0.02	2.55 ± 0.03	0.94/74
48	80146-01-59-00	6560	5.25 ± 0.02	1.16 ± 0.02	2.63 ± 0.05	0.84/74
49	80146-01-60-00	6832	5.36 ± 0.02	1.17 ± 0.02	2.57 ± 0.04	1.28/74
50	80146-01-62-00	2912	4.51 ± 0.02	1.13 ± 0.02	2.57 ± 0.04	0.59/74
51	80146-01-65-00	4496	4.96 ± 0.01	1.14 ± 0.02	2.60 ± 0.03	0.93/74
52	80146-01-66-00	4160	5.15 ± 0.02	1.13 ± 0.02	2.59 ± 0.02	0.79/74

Continued on next page

Table 3 – continued from previous page

#	ID	Exposure (s)	Frequency (Hz)	kT_{in} (keV)	Γ	χ^2/ν
53	80146-01-67-00	6112	5.19 ± 0.01	1.13 ± 0.02	2.59 ± 0.04	0.91/74
54	80146-01-68-00	6544	5.23 ± 0.03	1.12 ± 0.02	2.58 ± 0.02	0.90/74
55	80146-01-69-00	4928	5.25 ± 0.02	1.11 ± 0.02	2.59 ± 0.02	0.97/74
56	94413-01-03-02	1392	3.71 ± 0.03	1.07 ± 0.04	2.22 ± 0.05	1.06/47
57	94413-01-03-03	1680	3.72 ± 0.02	1.08 ± 0.03	2.24 ± 0.04	1.04/47
58	95360-14-04-00	2816	3.57 ± 0.01	1.06 ± 0.04	2.22 ± 0.03	1.16/47
59	96425-01-03-00	1744	3.53 ± 0.01	1.04 ± 0.04	2.19 ± 0.04	0.81/47
60	96425-01-03-02	1344	3.30 ± 0.02	0.99 ± 0.03	2.16 ± 0.05	1.10/47
61	96425-01-03-05	1072	3.49 ± 0.01	1.03 ± 0.05	2.19 ± 0.05	0.73/47
XTE J1550–564						
62	30191-01-32-00	880	5.49 ± 0.01	1.06 ± 0.02	2.44 ± 0.02	1.05/74
63	30191-01-33-00	9264	5.40 ± 0.01	1.05 ± 0.02	2.42 ± 0.01	1.48/74
64	30191-01-34-01	1136	4.93 ± 0.01	1.02 ± 0.02	2.37 ± 0.02	1.03/74
65	40401-01-50-00	3104	5.75 ± 0.03	1.06 ± 0.01	2.37 ± 0.02	1.40/74
66	40401-01-51-01	1120	5.93 ± 0.01	1.10 ± 0.02	2.48 ± 0.02	0.78/74
67	40401-01-53-00	2256	6.33 ± 0.01	1.10 ± 0.03	2.53 ± 0.02	0.97/74
68	40401-01-55-00	2448	6.13 ± 0.01	1.09 ± 0.02	2.48 ± 0.01	1.07/74
69	40401-01-56-00	544	6.14 ± 0.02	1.08 ± 0.03	2.46 ± 0.03	0.86/74
70	40401-01-56-01	192	6.16 ± 0.04	1.05 ± 0.03	2.48 ± 0.04	1.01/74
71	40401-01-58-00	1008	5.52 ± 0.01	1.04 ± 0.02	2.39 ± 0.02	0.96/74
72	40401-01-58-01	3456	5.98 ± 0.03	0.91 ± 0.02	2.37 ± 0.01	1.12/74
XTE J1859+226						
73	40122-01-01-00	6944	5.96 ± 0.01	1.01 ± 0.03	2.53 ± 0.01	0.59/74
74	40122-01-01-02	2240	5.97 ± 0.01	1.00 ± 0.03	2.53 ± 0.02	0.83/74
75	40122-01-01-03	2496	5.97 ± 0.01	1.03 ± 0.03	2.51 ± 0.02	0.91/74
76	40124-01-13-00	1760	6.10 ± 0.01	1.03 ± 0.03	2.52 ± 0.02	1.13/74
77	40124-01-24-00	2032	5.82 ± 0.02	0.98 ± 0.04	2.47 ± 0.02	0.81/74
78	40124-01-27-00	1184	5.87 ± 0.03	0.98 ± 0.04	2.44 ± 0.03	0.73/74
79	40124-01-30-00	2624	5.17 ± 0.01	0.86 ± 0.03	2.46 ± 0.02	0.88/74
80	40124-01-36-00	7520	4.70 ± 0.02	0.94 ± 0.03	2.38 ± 0.02	0.42/74
81	40124-01-37-00	2704	4.71 ± 0.01	0.92 ± 0.03	2.38 ± 0.02	0.98/74
82	40124-01-37-01	2080	4.54 ± 0.01	0.93 ± 0.03	2.35 ± 0.02	0.73/74
83	40124-01-37-02	6288	4.43 ± 0.01	0.92 ± 0.02	2.35 ± 0.02	0.51/74
84	40124-01-39-00	5840	5.63 ± 0.01	0.86 ± 0.01	2.26 ± 0.03	0.88/74
85	40124-01-40-00	1392	5.25 ± 0.01	0.86 ± 0.01	2.24 ± 0.05	0.64/74
86	40124-01-41-00	2912	4.78 ± 0.05	0.84 ± 0.01	2.23 ± 0.05	0.84/74
XTE J1752–223						
87	95360-01-01-00	2336	3.51 ± 0.01	0.68 ± 0.02	2.30 ± 0.03	0.73/74
XTE J1817–330						
88	91110-02-05-00	1728	5.46 ± 0.03	0.99 ± 0.01	2.55 ± 0.05	1.32/74
89	91110-02-07-00	3392	5.41 ± 0.02	0.98 ± 0.01	2.56 ± 0.05	0.96/74
90	91110-02-17-00	5808	4.80 ± 0.06	0.89 ± 0.01	2.39 ± 0.05	0.74/74
91	91110-02-18-00	7952	5.04 ± 0.03	0.88 ± 0.01	2.36 ± 0.04	0.74/74
92	91110-02-24-00	3888	5.30 ± 0.05	0.84 ± 0.01	2.33 ± 0.05	0.74/74
93	91110-02-29-00	1696	5.58 ± 0.02	0.87 ± 0.02	2.48 ± 0.03	0.85/47
94	91110-02-30-00	3200	5.61 ± 0.02	0.88 ± 0.03	2.43 ± 0.04	0.47/47
95	92082-01-02-03	1648	4.86 ± 0.13	0.85 ± 0.02	2.45 ± 0.04	0.84/47
MAXI J1659–152						
96	95118-01-01-01	3280	3.88 ± 0.01	0.89 ± 0.03	2.29 ± 0.03	0.73/47
97	95118-01-02-00	3216	3.46 ± 0.04	0.88 ± 0.02	2.29 ± 0.02	0.66/47
98	95118-01-07-00	3056	3.28 ± 0.02	0.83 ± 0.03	2.19 ± 0.05	0.81/47
99	95118-01-10-00	1088	3.54 ± 0.01	0.81 ± 0.04	2.13 ± 0.08	1.32/47

This paper has been typeset from a $\text{\TeX}/\text{\LaTeX}$ file prepared by the author.